J|A|C|S
ARTICLES
Published on Web 08/04/2006

From Homoligand- to Mixed-Ligand- Monolayer-Protected Metal Nanoparticles: A Scanning Tunneling Microscopy Investigation

Alicia M. Jackson, Ying Hu, Paulo Jacob Silva, and Francesco Stellacci*

Contribution from the Department of Materials Science and Engineering, Massachusetts Institute of Technology, Cambridge, Massachusetts 02139

Received March 13, 2006; E-mail: frstella@mit.edu

Abstract: The ligand shell that coats, protects, and imparts a large number of properties to gold nanoparticles is a 2-D self-assembled monolayer wrapped around a 3-D metallic core. Here we present a study of the molecular packing of ligand shells on gold nanoparticles based on the analysis of scanning tunneling microscopy (STM) images. We discuss methods for optimal nanoparticle sample preparation in relation to STM imaging conditions. We show that the packing of a self-assembled monolayer composed solely of octanethiols on gold nanoparticles depends on the particle's diameter with an average headgroup spacing of 5.4 Å, which is different from that of similar monolayers formed on flat Au(111) surfaces (5.0 Å). In the case of nanoparticles coated with mixtures of ligands—known to phase separate into randomly shaped and ordered domains on flat surfaces—we find that phase separation leads to the formation of concentric, ribbonlike domains of alternating composition. The spacing of these domains depends on the ligand shell composition. We find that, for a given composition, the spacing increases with diameter in a manner characterized by discontinuous transitions at "critical" particle sizes. We discuss possible interpretations for the observed trends in our data.

1. Introduction

Monolayer-protected metal nanoparticles are supramolecular assemblies composed of a noble metal core surrounded by a self-assembled monolayer (SAM) of organic molecules, typically bound to the metal through a thiol−gold bond.[1−3] In recent years, they have been used in many fields of science from physics,[4,5] to chemistry,[6−9] to materials science,[10−12] to biology,[13−15] and all the way to medicine.[16−18] This is primarily due to the simplicity of their synthesis[1,19] and to their unique optical[3,20] and electronic[21] properties that depend strongly on size and shape.[22−26] Additionally, a true strength of gold and silver nanoparticles lies in the ease (at least relative to other nanoscale materials) with which a wide variety of different thiolated molecules can be placed in the ligand shell either by direct synthesis methods[3,19,27,28] or by place-exchange reactions.[1,29−32] The protecting monolayer, i.e., the ligand shell,

(1) Templeton, A. C.; Wuelfing, M. P.; Murray, R. W. *Acc. Chem. Res.* **2000**, *33*, 27−36.
(2) Daniel, M. C.; Astruc, D. *Chem. Rev.* **2004**, *104*, 293−346.
(3) Thomas, K. G.; Kamat, P. V. *Acc. Chem. Res.* **2003**, *36*, 888−898.
(4) Andres, R. P.; Bein, T.; Dorogi, M.; Feng, S.; Henderson, J. I.; Kubiak, C. P.; Mahoney, W.; Osifchin, R. G.; Reifenberger, R. *Science* **1996**, *272*, 1323−1325.
(5) Andres, R. P.; Bielefeld, J. D.; Henderson, J. I.; Janes, D. B.; Kolagunta, V. R.; Kubiak, C. P.; Mahoney, W. J.; Osifchin, R. G. *Science* **1996**, *273*, 1690−1693.
(6) Chen, S. W.; Ingram, R. S.; Hostetler, M. J.; Pietron, J. J.; Murray, R. W.; Schaaff, T. G.; Khoury, J. T.; Alvarez, M. M.; Whetten, R. L. *Science* **1998**, *280*, 2098−2101.
(7) Green, S. J.; Pietron, J. J.; Stokes, J. J.; Hostetler, M. J.; Vu, H.; Wuelfing, W. P.; Murray, R. W. *Langmuir* **1998**, *14*, 5612−5619.
(8) Hicks, J. F.; Zamborini, F. P.; Osisek, A.; Murray, R. W. *J. Am. Chem. Soc.* **2001**, *123*, 7048−7053.
(9) Ingram, R. S.; Murray, R. W. *Langmuir* **1998**, *14*, 4115−4121.
(10) Shevchenko, E. V.; Talapin, D. V.; Kotov, N. A.; O'Brien, S.; Murray, C. B. *Nature* **2006**, *439*, 55−59.
(11) Collier, C. P.; Vossmeyer, T.; Heath, J. R. *Annu. Rev. Phys. Chem.* **1998**, *49*, 371−404.
(12) Akthakul, A.; Hochbaum, A. I.; Stellacci, F.; Mayes, A. M. *Adv. Mater.* **2005**, *17*, 532−539.
(13) You, C. C.; De, M.; Han, G.; Rotello, V. M. *J. Am. Chem. Soc.* **2005**, *127*, 12873−12881.
(14) You, C. C.; De, M.; Rotello, V. M. *Curr. Opin. Chem. Biol.* **2005**, *9*, 639−646.
(15) Shipway, A. N.; Katz, E.; Willner, I. *ChemPhysChem* **2000**, *1*, 18−52.
(16) Veiseh, O.; Sun, C.; Gunn, J.; Kohler, N.; Gabikian, P.; Lee, D.; Bhattarai, N.; Ellenbogen, R.; Sze, R.; Hallahan, A.; Olson, J.; Zhang, M. Q. *Nano Lett.* **2005**, *5*, 1003−1008.
(17) Georganopoulou, D. G.; Chang, L.; Nam, J. M.; Thaxton, C. S.; Mufson, E. J.; Klein, W. L.; Mirkin, C. A. *Proc. Natl. Acad. Sci. U.S.A.* **2005**, *102*, 2273−2276.
(18) Han, G.; Chari, N. S.; Verma, A.; Hong, R.; Martin, C. T.; Rotello, V. M. *Bioconjugate Chem.* **2005**, *16*, 1356−1359.
(19) Brust, M.; Walker, M.; Bethell, D.; Schiffrin, D. J.; Whyman, R. *J. Chem. Soc., Chem. Commun.* **1994**, 801−802.
(20) Malinsky, M. D.; Kelly, K. L.; Schatz, G. C.; Van Duyne, R. P. *J. Am. Chem. Soc.* **2001**, *123*, 1471−1482.
(21) Collier, C. P.; Saykally, R. J.; Shiang, J. J.; Henrichs, S. E.; Heath, J. R. *Science* **1997**, *277*, 1978−1981.
(22) Hostetler, M. J.; Wingate, J. E.; Zhong, C. J.; Harris, J. E.; Vachet, R. W.; Clark, M. R.; Londono, J. D.; Green, S. J.; Stokes, J. J.; Wignall, G. D.; Glish, G. L.; Porter, M. D.; Evans, N. D.; Murray, R. W. *Langmuir* **1998**, *14*, 17−30.
(23) Feldheim, D. L.; Keating, C. D. *Chem. Soc. Rev.* **1998**, *27*, 1−12.
(24) McConnell, W. P.; Novak, J. P.; Brousseau, L. C.; Fuierer, R. R.; Tenent, R. C.; Feldheim, D. L. *J. Phys. Chem. B* **2000**, *104*, 8925−8930.
(25) Link, S.; El-Sayed, M. A. *J. Phys. Chem. B* **1999**, *103*, 8410−8426.
(26) Link, S.; El-Sayed, M. A. *J. Phys. Chem. B* **1999**, *103*, 4212−4217.
(27) Stellacci, F.; Bauer, C. A.; Meyer-Friedrichsen, T.; Wenseleers, W.; Alain, V.; Kuebler, S. M.; Pond, S. J. K.; Zhang, Y. D.; Marder, S. R.; Perry, J. W. *Adv. Mater.* **2002**, *14*, 194−198.
(28) Stellacci, F.; Meyer-Friedrichsen, T.; Bauer, C. A.; Wenseleers, W.; Marder, S. R.; Perry, J. W. *J. Am. Chem. Soc.* **2003**, *125*, 328−328.
(29) Hostetler, M. J.; Green, S. J.; Stokes, J. J.; Murray, R. W. *J. Am. Chem. Soc.* **1996**, *118*, 4212−4213.
(30) Ingram, R. S.; Hostetler, M. J.; Murray, R. W. *J. Am. Chem. Soc.* **1997**, *119*, 9175−9178.

serves a critical role, providing the particles with a long series of properties, to name a few, stability against coalescence,[33] solubility in many solvents,[34,35] assembly properties,[36] electrochemical charging,[7] electron-transfer efficiency,[33,37] sensing of specific biomolecules,[13,38] and pseudoenzymatic activity.[39−45] Basically, the ligand shell controls and rules all of the interactions of the particles with the outside molecular world; thus, a complete list would go beyond the scope of this paper.

Very often in engineering the properties of nanoparticles only the molecular functionalities of the ligand molecules are taken into account and studied. However, it is becoming increasingly evident that ligand shell morphology plays just as important a role.[36,46−49] Molecular packing and conformation and shell composition have been studied thoroughly using FTIR,[22,46] NMR,[22] neutron scattering,[50] and HPLC,[51] and it has been shown that SAMs on nanoparticles are at least as ordered as SAMs on flat surfaces.[22,52,53] Additionally, molecular dynamics calculations have been performed to investigate how such a 2-D crystalline SAM can order itself around a curved (in a topological sense; the faceted crystalline core is topologically equivalent, or homeomorphic, to a sphere: that is, the polyhedral core can be deformed through a bicontinuous transformation, i.e., stretching without tearing or gluing, into a sphere; thus, those topological principals which hold for spheres will hold for all homeomorphs of the sphere[54]), 3-D nanoparticle core, often with a radius of curvature comparable to the length of the molecules.[55,56] Still, at present, we lack an understanding of how ligands organize around the topological sphere that is the particle's metallic core while keeping a high degree of order and packing density. Indeed, ligand shells (frequently referred to as 3-D monolayers)[22] are subject to constraints not found in the 2-D case—such as the 2π rotational symmetry of the nanoparticle core. The packing of objects around a sphere has long been an area of scientific study from the Thompson problem of the distribution of charges on a sphere[57] to the packing of proteins in the capsid shell of a virus[58,59] and has been shown to give rise to many interesting surface features and functionalities.[60−62] Thus, it would not be unexpected to find such unique ordering and packing of molecules around the nanoparticle core.

Here we present a scanning tunneling microscopy (STM) study of monolayer-protected nanoparticles aimed at probing ligand organization with what is probably the only microscopy technique that has the capability of visualizing these molecules. When intrinsically polydisperse samples such as nanoparticles are being studied, STM, being a microscopy tool, has the distinct advantage of providing single-particle data as opposed to the average ensemble data that spectroscopy techniques produce.[63−66] However, STM imaging of nanoparticles with molecular resolution is nontrivial and, being a microscopy tool, needs averaging over multiple images to result in representative data. We find that octanethiol-coated nanoparticles show an average headgroup spacing of 5.4 Å which, importantly, seems to increase with nanoparticle diameter. It should be noted that, on flat Au(111), octanethiol monolayers have a constant headgroup spacing of 5.0 Å (see the Discussion).

Furthermore, we studied ligand packing on mixed-ligand octanethiol/mercaptopropionic acid nanoparticles. We recently presented what is probably the first significant difference in the morphology of SAMs on nanoparticles when compared to SAMs of the same composition on flat surfaces.[67] It was known that some SAMs composed of mixtures of ligands phase separate into randomly sized and shaped domains.[68−71] We found that those SAMs phase separate into ordered, ribbonlike domains of alternating composition that encircle or spiral around the nanoparticle core (Figure 1). We have evidence that suggests that the topological curvature (present in the core) is the driving force for the ordering of these phases.[67] Interestingly, the width of these phases was found to be extremely small, often no more than two molecules.[67] This unprecedented small size of the

(31) Song, Y.; Huang, T.; Murray, R. W. *J. Am. Chem. Soc.* **2003**, *125*, 11694−11701.
(32) Templeton, A. C.; Hostetler, M. J.; Kraft, C. T.; Murray, R. W. *J. Am. Chem. Soc.* **1998**, *120*, 1906−1911.
(33) Terrill, R. H.; Postlethwaite, T. A.; Chen, C. H.; Poon, C. D.; Terzis, A.; Chen, A. D.; Hutchison, J. E.; Clark, M. R.; Wignall, G.; Londono, J. D.; Superfine, R.; Falvo, M.; Johnson, C. S.; Samulski, E. T.; Murray, R. W. *J. Am. Chem. Soc.* **1995**, *117*, 12537−12548.
(34) Levy, R.; Thanh, N. T. K.; Doty, R. C.; Hussain, I.; Nichols, R. J.; Schiffrin, D. J.; Brust, M.; Fernig, D. G. *J. Am. Chem. Soc.* **2004**, *126*, 10076−10084.
(35) Lucarini, M.; Franchi, P.; Pedulli, G. F.; Gentilini, C.; Polizzi, S.; Pengo, P.; Scrimin, P.; Pasquato, L. *J. Am. Chem. Soc.* **2005**, *127*, 16384−16385.
(36) Glotzer, S. C. *Science* **2004**, *306*, 419−420.
(37) Chen, S. W. *J. Electroanal. Chem.* **2004**, *574*, 153−165.
(38) Chen, Y.; Aveyard, J.; Wilson, R. *Chem. Commun.* **2004**, 2804−2805.
(39) Pasquato, L.; Pengo, P.; Scrimin, P. *Supramol. Chem.* **2005**, *17*, 163−171.
(40) Briggs, C.; Norsten, T. B.; Rotello, V. M. *Chem. Commun.* **2002**, 1890−1891.
(41) Lucarini, M.; Franchi, P.; Pedulli, G. F.; Pengo, P.; Scrimin, P.; Pasquato, L. *J. Am. Chem. Soc.* **2004**, *126*, 9326−9329.
(42) Manea, F.; Houillon, F. B.; Pasquato, L.; Scrimin, P. *Angew. Chem., Int. Ed.* **2004**, *43*, 6165−6169.
(43) Pasquato, L.; Pengo, P.; Scrimin, P. *J. Mater. Chem.* **2004**, *14*, 3481−3487.
(44) Verma, A.; Nakade, H.; Simard, J. M.; Rotello, V. M. *J. Am. Chem. Soc.* **2004**, *126*, 10806−10807.
(45) Verma, A.; Simard, J. M.; Worrall, J. W. E.; Rotello, V. M. *J. Am. Chem. Soc.* **2004**, *126*, 13987−13991.
(46) Paulini, R.; Frankamp, B. L.; Rotello, V. M. *Langmuir* **2002**, *18*, 2368−2373.
(47) Zhang, Z. L.; Glotzer, S. C. *Nano Lett.* **2004**, *4*, 1407−1413.
(48) Shenhar, R.; Rotello, V. M. *Acc. Chem. Res.* **2003**, *36*, 549−561.
(49) Love, J. C.; Estroff, L. A.; Kriebel, J. K.; Nuzzo, R. G.; Whitesides, G. M. *Chem. Rev.* **2005**, *105*, 1103−1169.
(50) Pradeep, T.; Mitra, S.; Nair, A. S.; Mukhopadhyay, R. *J. Phys. Chem. B* **2004**, *108*, 7012−7020.
(51) Song, Y.; Heien, M. L. A. V.; Jimenez, V.; Wightman, R. M.; Murray, R. W. *Anal. Chem.* **2004**, *76*, 4911−4919.
(52) Badia, A.; Cuccia, L.; Demers, L.; Morin, F.; Lennox, R. B. *J. Am. Chem. Soc.* **1997**, *119*, 2682−2692.
(53) Hostetler, M. J.; Stokes, J. J.; Murray, R. W. *Langmuir* **1996**, *12*, 3604−3612.
(54) Hocking, J. G.; Young, G. S. *Topology*; Dover: New York, 1988.
(55) Luedtke, W. D.; Landman, U. *J. Phys. Chem. B* **1998**, *102*, 6566−6572.
(56) Gutierrez-Wing, C.; Ascencio, J. A.; Perez-Alvarez, M.; Marin-Almazo, M.; Jose-Yacaman, M. *J. Cluster Sci.* **1998**, *9*, 529−545.
(57) Thompson, J. J. *Philos. Mag.* **1904**, *7*, 237.
(58) Reddy, V. S.; Natarajan, P.; Okerberg, B.; Li, K.; Damodaran, K. V.; Morton, R. T.; Brooks, C.; Johnson, J. E. *J. Virol.* **2001**, *75*, 11943−11947.
(59) Marzec, C. J.; Day, L. A. *Biophys. J.* **1993**, *65*, 2559−2577.
(60) Bausch, A. R.; Bowick, M. J.; Cacciuto, A.; Dinsmore, A. D.; Hsu, M. F.; Nelson, D. R.; Nikolaides, M. G.; Travesset, A.; Weitz, D. A. *Science* **2003**, *299*, 1716−1718.
(61) Nelson, D. R. *Nano Lett.* **2002**, *2*, 1125−1129.
(62) Li, C. R.; Zhang, X. O.; Cao, Z. X. *Science* **2005**, *310*, 236−236.
(63) Bigioni, T. P.; Harrell, L. E.; Cullen, W. G.; Guthrie, D. E.; Whetten, R. L.; First, P. N. *Eur. Phys. J. D* **1999**, *6*, 355−364.
(64) Harrell, L. E.; Bigioni, T. P.; Cullen, W. G.; Whetten, R. L.; First, P. N. *J. Vac. Sci. Technol., B* **1999**, *17*, 2411−2416.
(65) Rolandi, M.; Scott, K.; Wilson, E. G.; Meldrum, F. C. *J. Appl. Phys.* **2001**, *89*, 1588−1595.
(66) Li, J.; Liang, K. S.; Camillone, N.; Leung, T. Y. B.; Scoles, G. *J. Chem. Phys.* **1995**, *102*, 5012−5028.
(67) Jackson, A. M.; Myerson, J. W.; Stellacci, F. *Nat. Mater.* **2004**, *3*, 330−336.
(68) Stranick, S. J.; Atre, S. V.; Parikh, A. N.; Wood, M. C.; Allara, D. L.; Winograd, N.; Weiss, P. S. *Nanotechnology* **1996**, *7*, 438−442.
(69) Folkers, J. P.; Laibinis, P. E.; Whitesides, G. M. *Langmuir* **1992**, *8*, 1330−1341.
(70) Smith, R. K.; Reed, S. M.; Lewis, P. A.; Monnell, J. D.; Clegg, R. S.; Kelly, K. F.; Bumm, L. A.; Hutchison, J. E.; Weiss, P. S. *J. Phys. Chem. B* **2001**, *105*, 1119−1122.
(71) Delamarche, E.; Michel, B.; Biebuyck, H. A.; Gerber, C. *Adv. Mater.* **1996**, *8*, 719−729.

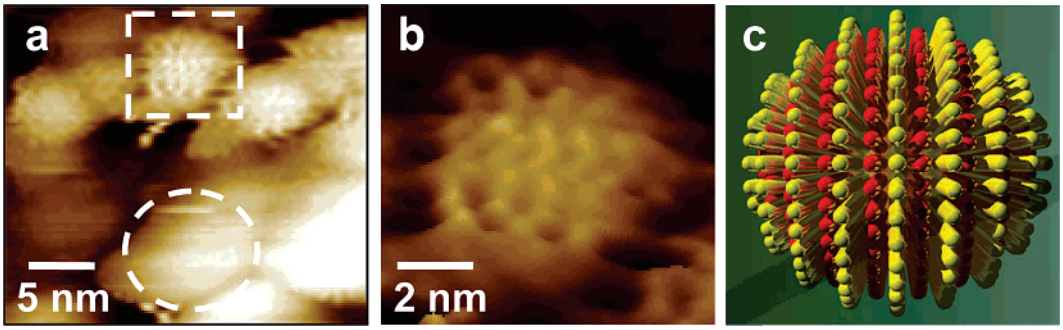

Figure 1. (a) STM height image of gold nanoparticles, on Au foil, coated with a 2:1 molar ratio of OT and MPA showing ribbonlike stripes, hereafter called ripples, due to the phase separation of the two ligands. One such particle is outlined by the dotted square and shown in an enlarged image in (b). The raised domains that run across the particles are the OT phases which alternate with the MPA phases. A schematic drawing to help the reader visualize this 3-D arrangement is shown in (c). A feature that one should recognize in the image is that, while in some areas (such as the one demarcated by the dashed white circle) the underlying gold foil exhibits a curvature comparable to that of the nanoparticles, no hint of ripples is observed, indicating that ripples are not the result of the STM tip scanning over an area of high curvature.

phases leads to unexpected properties of the nanoparticles such as a nonmonotonic dependence on composition of solubility and good resistance to protein nonspecific adsorption.[67] Here we present an analysis of STM images of nanoparticles coated with a mixture of octanethiol (OT) and mercaptopropionic acid (MPA) (in 2:1 and 1:1 molar ratios) together with new data that correlate the domain spacing with the particles' diameter. We find that the domain spacing increases with diameter. The relevance of these data in terms of ligand morphology and packing is discussed.

The paper is organized as follows: In section 2 (Experimental Methods) we present the experimental details of sample preparation and STM imaging. In section 3 (Results) we first discuss the challenges of STM imaging and the interpretation of the STM images and then present data on the domain spacing dependence on particle diameter for various particle compositions. Finally, in section 4 (Discussion) we present possible interpretation models to understand our results. The final two sections are the Conclusions and Experimental Section.

2. Experimental Methods

2.1. Nanoparticle Synthesis. Au nanoparticles were synthesized using either a two-phase[19] or a one-phase[72] synthesis method. The two-phase synthesis was performed using a slight variation of the Schriffin method.[19] Typically 0.9 mmol of a gold salt ($HAuCl_4 \cdot 3H_2O$) in 50 mL of water was transferred into an organic phase (80 mL of toluene) using a 4-fold excess of a phase-transfer agent (tetraoctylammonium bromide, (TOA)Br). A 0.9 mmol portion of the thiolated molecule (or a mixture of thiolated molecules) was added, followed by dropwise addition of a reducing agent ($NaBH_4$ (10 mmol)) in 30 mL of water. The phases were separated, and the organic phase was reduced to 10 mL and diluted with ~80 mL of ethanol. The solution was stored in the refrigerator overnight to allow for the nanoparticles to slowly precipitate, then filtered, and washed extensively with water, ethanol, acetonitrile, and acetone. The cleaning procedure is of fundamental importance to obtain STM images that show molecular resolution of the ligand shell packing, as during STM imaging any impurity within or surrounding the ligand shell will obscure the whole particle image and can potentially contaminate the microscope tip. A description of each particle's synthesis and purification can be found in the Experimental Section.

In the one-phase method, 0.9 mmol of $HAuCl_4 \cdot 3H_2O$ was dissolved in 200 mL of ethanol at 0 °C. A 0.9 mmol portion of the thiolated molecule (or a mixture of thiolated molecules) was added and allowed to react. A 200 mL portion of a supersaturated solution of $NaBH_4$ in ethanol was then added dropwise. After complete addition, the solution was stirred for 2 h and then transferred to the refrigerator to slowly precipitate. The particles were then filtered and cleaned as described for the two-phase synthesis. This method has the advantage of not requiring a phase-transfer agent ((TOA)Br)—typically difficult to fully eliminate from the particle's ligand shell.[73]

In the case of mixed-ligand nanoparticles the total number of moles of organic was kept constant (0.9 mmol) but various molar ratios were used. It was always assumed that the stoichiometric ratio of the ligands in solution was equal to the ratio on the ligand shell. Recent bulk FTIR studies of OT/MPA mixed-ligand nanoparticles confirm this assumption.[74] Throughout the paper the ratio indicated will always be the stoichiometric molar ratio.

Both types (one-phase or two-phase) of nanoparticles were imaged using STM. Each synthesis resulted in samples of nanoparticles polydisperse in size, with a core diameter of ~4 nm dominating the distribution.

2.2. Nanoparticle Monolayer Preparation for STM Imaging. To immobilize the nanoparticles on gold substrates so that they are not free to move during imaging, dithiol molecules were used to act as linkers, binding the nanoparticles to the underlying substrate and sometimes to one another, creating a dense network of nanoparticles. Briefly, a SAM of 1,8-octanedithiol (ODiT) was first formed by immersing the substrate in a 200 μM ethanolic solution, followed by thorough rinsing. A 2 mg portion of nanoparticles dissolved in 10 mL of the appropriate solvent (e.g., toluene or ethanol depending on the nanoparticle solubility) was then cast onto the substrate and allowed to slowly evaporate in the presence of a saturated solvent atmosphere (note that the substrate must be level to allow for even evaporation). Alternatively, equivalent samples could also be prepared by simply immersing the substrate in 20 mL of a 5.6×10^{-2} mM toluene solution of ODiT containing 2 mg of nanoparticles for 24 h. All samples were cleaned by rinsing with toluene, then incubating (and, in the case of Au foil, cleaning with mild sonication) in ethanol for several hours, and drying under a stream of nitrogen.

Recently, we have developed a new sample preparation method that results in more consistent nanoparticle layers. (Note that we have applied the procedure to only OT homoligand and OT/MPA (2:1) rippled nanoparticles.) For OT/MPA (2:1) nanoparticles, a SAM of butanethiol was first formed by immersing the substrate in a 100 μM ethanolic solution for ~24 h prior to nanoparticle layer formation, after which it was immediately rinsed and stored in ethanol. A ~3 mg portion of nanoparticles was dissolved in 1 mL of toluene. A 40 times excess of 1,10-decanedithiol (DdiT) in 0.5 mL of toluene was then added to

(72) Kang, S. Y.; Kim, K. *Langmuir* **1998**, *14*, 226−230.

(73) Waters, C. A.; Mills, A. J.; Johnson, K. A.; Schiffrin, D. J. *Chem. Commun.* **2003**, 540−541.

(74) Centrone, A.; Pawloski, A.; Zerbi, G.; Stellacci, F. Manuscript in preparation.

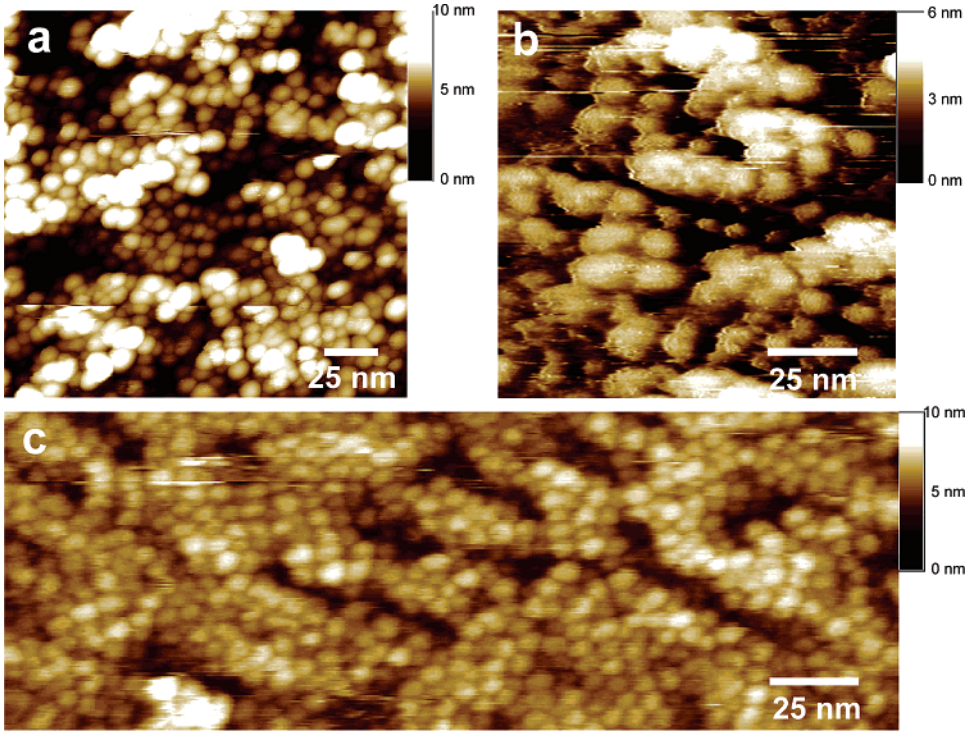

Figure 2. STM images illustrating the differences in nanoparticle film morphologies as a result of the underlying substrate used. Nanoparticle films were formed on (a) Au foil (large height variations are evident), (b) Au(111) on mica (more isolated particles and islands of aggregates of particles can be seen), and (c) Au on glass (a nearly uniform film of hexagonally packed nanoparticles can be observed). Streakiness in the images (particularly in (c)) is attributed to molecular impurities within the monolayer. Nanoparticles in (a) and (c) were synthesized using the two-phase method with a ligand ratio of 2:1 nonanethiol/mercaptohexanol. Nanoparticles in (b) were synthesized using the one-phase method with a ligand ratio of 2:1 OT/MPA.

the nanoparticles and the solution incubated for 30 min to allow for place exchange of the DdiT into the ligand shell. The foil was immersed into the solution and allowed to incubate for 5 h. The sample was rinsed in toluene for 5 min, then immersed into hot (∼85 °C) toluene for 20 min, and, finally, rinsed with acetonitrile and dried under nitrogen. For OT homoligand nanoparticles the sample preparation was essentially the same; however, ∼5 mg/mL toluene solutions were used and the nanoparticles incubated with DdiT for 40 min.

2.3. Substrates. Three types of substrates were used to image the particles: Au foil, Au(111) thermally evaporated on freshly cleaved mica, and Au on glass prepared using the method developed by Ulman and co-workers.[75] Au foil is an inexpensive and easy to clean (via mild sonication) substrate. It is flat only locally and has numerous scratches. Au(111) on mica is flat over the numerous ∼100 nm large terraces but cannot be cleaned easily (sonication promotes delamination and small fractures). Au on glass, which presents a nearly impurity free surface, is obtained by placing a Au on mica substrate facedown onto a glass slide coated with an epoxy resin, sandwiching the Au film between the glass and the mica.[75] The mica is then removed by placing the sample in an ethanol solution containing ODiT, so that the molecules intercalcate between the gold and the mica, separating the two surfaces and forming a SAM. The resulting gold surface is flat over large terraces and, importantly, very clean[76] because it was coated with a monolayer while being delaminated. However, we should point out that for nanoparticle imaging this substrate is problematic because cleaning after nanoparticle deposition is challenging. In fact, in our experience, it is not possible to immerse the sample in many solvents because the epoxy resin either swells or, more often, releases impurities that contaminate the substrate and render high-resolution imaging problematic. Nanoparticle assemblies on these three substrates seem to be very different and present different imaging challenges according to each substrate as discussed in the Results.

2.4. STM Imaging. A Digital Instruments Multimode Nanoscope IIIa-E scanner with mechanically cut platinum−iridium tips was used to obtain all of the images in this paper. The tip bias used was typically between 900 and 1300 mV with set currents of 600−800 pA. We have noticed that the best and most crisp (i.e., noise-free) images obtained are at tip speeds between 0.4 and 1.4 μm/s; occasionally good images at lower (as low as 0.2 μm/s) or higher (as high as 2.0 μm/s) speeds have been obtained. It should be noted that the image quality is often dependent on the scan parameters; in particular, large changes in tip speed can result in loss of resolution. The integral gain used to obtain these images was in the range of 0.3−0.65, with the proportional being roughly half to two-thirds of that value.

3. Results

3.1. STM Imaging of Substrates. Using STM, it was observed that the three substrates, Au foil, Au(111) on mica, and Au on glass, resulted in very different nanoparticle layer morphologies. It was consistently noted that when using Au foil that the nanoparticles formed irregular layers, often with large variations in overall film height (Figure 2a). Poor overall sample flatness can sometimes lead to noisy imaging conditions, complicating ligand shell imaging. On Au(111) on mica only sparse islands of nanoparticle aggregates and isolated nanoparticles were observed, and many times, no nanoparticles were visible at all (Figure 2b). The abrupt height changes from the terraces to the curved nanoparticles often resulted in noisy regions surrounding the nanoparticles, making precise imaging of the ligand shell difficult. We believe that the lack of large areas of densely packed nanoparticles is due to surface contamination. Indeed, often different monolayer morphologies

(75) Gupta, P.; Loos, K.; Korniakov, A.; Spagnoli, C.; Cowman, M.; Ulman, A. *Angew. Chem., Int. Ed.* **2004**, *43*, 520−523.
(76) Gupta, P.; Ulman, A.; Fanfan, S.; Korniakov, A.; Loos, K. *J. Am. Chem. Soc.* **2005**, *127*, 4−5.

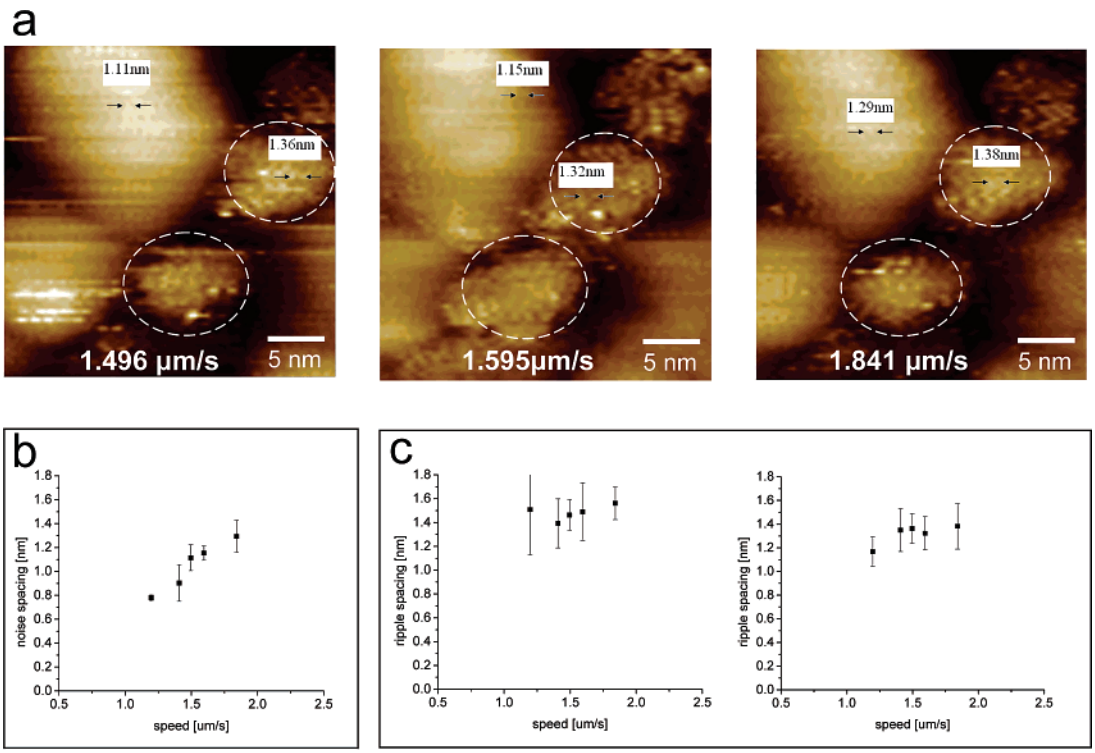

Figure 3. (a) STM images of two (circled) OT/MPA (2:1) gold nanoparticles cast onto a gold foil substrate. These images show how, at times, ripples can look similar to noise in our images, but when images taken at different tip speeds are compared, it is apparent that ripple spacing remains constant while noise spacing scales linearly with speed. Spacing measurements at three different tip speeds for one of the nanoparticles and for the gold foil are indicated in the three images. (b, c) Spacing measurements as a function of tip speed (b) for the noise and (c) for the ripples of each particle. It is immediately obvious how different the behavior is in the two regions. Also, it was noted that the amplitude (height from peak to trough) of the ripples was somehow greater than that of the noise. Being that the measurements are taken on the same images, effects of gains and other imaging parameters are excluded. Each point in the plots is the average of multiple measurements; the calculated standard deviations are shown as error bars in the plot.

were obtained on different Au on mica sample batches despite efforts to keep the sample preparation procedures identical. In contrast, samples prepared on Au on glass resulted in large-scale domains (>500 nm) of roughly hexagonally packed nanoparticles, one monolayer thick, the nanoparticles being of approximately the same size within each domain (although the nanoparticle size between domains varied) (Figure 2c). Often these layers showed contaminations that, during the cleaning procedure, were transferred from the epoxy adhesion layer. It was found that our best images were obtained on Au foil due to the improved ability to remove contaminants from the monolayer, as compared to alternative substrates.

3.2. Imaging of Nanoparticles. In this paper a careful analysis of the structure and the ordering of molecules on metal nanoparticles is presented. STM, as with any other scanning probe technique, is subject to imaging artifacts, and care must be taken to mitigate and to recognize such artifacts. Images of nanoparticles and their ligand shell were obtained at various tip speeds to verify that the features observed on the particles reflected the true molecular configuration and were not noise or a convolution of noise and reality. In most images we found both regions with tip-speed-*dependent* features (typically when imaging the substrate) and regions with tip-speed-*independent* features (typically when imaging the nanoparticles)—the former being noise related, the latter being the true molecular packing. A clear example of this is illustrated in Figure 3 for OT/MPA (2:1) nanoparticles. Additionally, Figure 4 shows STM images of OT/MPA (1:1) nanoparticles which maintain the same ripple spacing when imaged at a tip velocity of 0.57 and 0.814 μm/s, and Figure 5 shows a similar experiment done on OT homoligand nanoparticles. Similar controls were done on all of the nanoparticles presented in this paper.

3.3. Homoligand Nanoparticles. We carried out an extensive study of homoligand nanoparticles to determine what role core curvature (in a topological sense; the faceted crystalline core is topologically equivalent, or homeomorphic, to a sphere[54]) plays in the packing arrangement and density of the ligands without the additional packing constraints added by phase separation. Au particles with a size distribution ranging from approximately 2 to 7 nm and coated with OT were synthesized using both one- and two-phase methods and imaged. Shown in Figures 5 and 6 are STM height images of such OT particles. The particles' ligand shells show striking morphological differences from mixed-ligand, rippled nanoparticles; they do not show the ribbonlike, phase-separated domains that are observed in the case of binary mixtures of ligands (see, for example, Figure 1) and are significantly more difficult to image due to the lack of height and chemical contrast between ligands. Their methyl headgroups are visible, with the molecules packing tightly around the core with a headgroup spacing of ~0.5 nm.

To correlate ligand packing to nanoparticle curvature, we first plotted the STM-observed headgroup spacing as a function of core diameter using several scan images of OT homoligand nanoparticles (Figure 7). The core diameter, d, was determined from the STM-observed nanoparticle diameter, D, minus twice the length, L, of the surrounding ligands, $d = D - 2L$. For a fully extended (all-trans) alkyl ligand chain with n carbon atoms, we used the relation $L = 0.12(n + 1)$ (nm) to estimate the

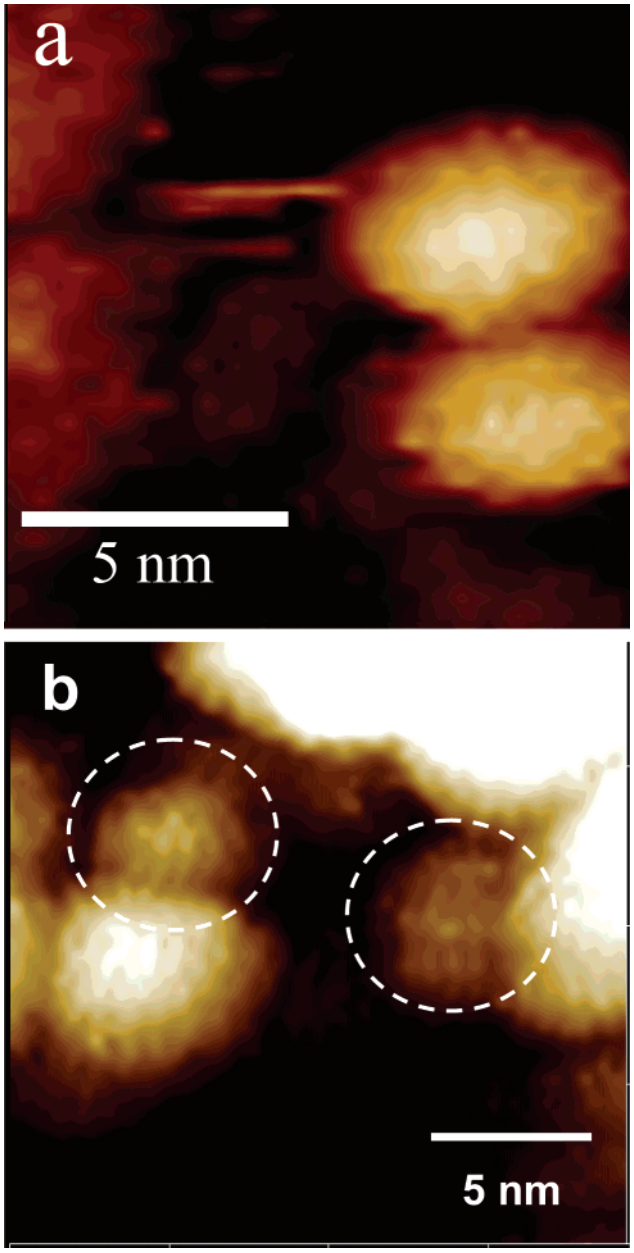

Figure 4. Comparison of ripple spacing of OT/MPA (1:1) nanoparticles imaged at varying tip speeds. (a) STM height image of a cluster of two nanoparticles showing ripples imaged at 0.57 μm/s. The top particle has a diameter of 5.1 nm and an average ripple spacing of 0.70 nm. The bottom particle has a diameter of 4.8 nm and a corresponding average ripple spacing of 0.67 nm. The total ensemble average ripple spacing for particles imaged is 0.67 nm. (b) STM height image of another cluster of nanoparticles imaged at 0.814 μm/s showing a spacing comparable to that in (a). The left, circled nanoparticle has an observed diameter of 4.2 nm and an average ripple spacing of 0.7 nm. The right, circled particle has an observed diameter of 6 nm and an average ripple spacing of 0.71 nm. The larger particle beneath the smaller, top left particle was not used to determine ripple spacing as its ripples are not easily discernible. It is likely that the nanoparticle is rotated with respect to the scan direction, thus obscuring the ripple direction. For an extended analysis of spacing measurements as a function of tip speed, see Figure 15.

molecular length.[77] The assumption that ligands on nanoparticles are mostly all trans is supported by FTIR data.[22] The headgroup spacings on each nanoparticle were determined by measuring the peak to peak spacing between clearly visible headgroups located near the center of the particle, generally measuring four or more spacings per particle. We believe that spacings taken at particle edges are more subject to tip/sample distortions and, due to geometric considerations, may not be representative of the actual molecular configurations. In most cases we tried to measure spacing between neighboring headgroups horizontally aligned to minimize the possibility of line scan artifacts or sample drift. The typical standard deviation of headgroup spacing on single nanoparticles ranged anywhere from 0.3 to 1 Å. While headgroup (or ripple, in the case of mixed-ligand particles) spacing can be measured with high accuracy, for diameter measurements, it was determined through multiple measurements on individual nanoparticles that the best achievable resolution was 0.2 nm. This is due to the fact that nanoparticle supracrystal images do not show clear boundaries between nanoparticles. Thus, nanoparticle diameters were expressed in nanometers with the first decimal digit (i.e., the last significant digit) rounded to the nearest odd number. The headgroup spacings shown in Figure 7b were calculated by averaging all of the measurements of spacings found for nanoparticles of a given diameter. At least three spacing measurements were made per particle. The plotted error bars in this measurement are ± 1 standard deviation of the averaged spacing measurements. It should be noted that the number of spacings averaged to obtain the data points in this paper varies, as smaller and larger particles were considerably less present on the sample when compared to those with average diameter. Also, sometimes, we have observed that particles of certain diameter are absent or rare in our images; this may be related to crystallographic reasons or to sample preparation issues. These conventions are used for all spacing plots throughout this paper, unless otherwise specified. Referring to Figure 7, the average headgroup spacing across all particles is 5.4 Å, with a slight increase in average spacing with increasing core diameter from a value of 5.0 Å at 2.7 nm diameter to 6.0 Å at 5.1 nm core diameter.

3.4. Mixed-Ligand Nanoparticles. 3.4.1. Image Interpretation. Images of mixed-ligand nanoparticles show ligand shell morphologies different from those of images of homoligand nanoparticles. We recently found that mixtures of thiolated ligands, that phase separate into randomly shaped domains when assembled on flat surfaces,[68−70] phase separate into ordered, ribbonlike domains when assembled on metal nanoparticles.[67] We do not expect to observe these ribbonlike domains for mixtures of molecules that do not phase separate on flat surfaces. Referring to Figure 1, the STM image shows gold nanoparticles coated with a 2:1 molar ratio of OT/MPA sparsely distributed on a Au foil substrate. As is observed in the image, molecular domains align into parallel, ribbonlike stripes that encircle and/or spiral around the nanoparticles. The spacing of the phases, measured as the average spacing between two peaks, is ~1 nm. At present we believe that the OT molecular domains are the bright, raised ripples, while the MPA molecular domains are located between those of the OT. This assignment is based on the analysis of STM images of OT/MPA SAMs on flat surfaces of varying composition: as the OT fraction decreases so does the fraction of "high" domains.

A feature that one should recognize in the image of the nanoparticles is that while in some areas the underlying gold

(77) Whetten, R. L.; Shafigullin, M. N.; Khoury, J. T.; Schaaff, T. G.; Vezmar, I.; Alvarez, M. M.; Wilkinson, A. *Acc. Chem. Res.* **1999**, *32*, 397−406.

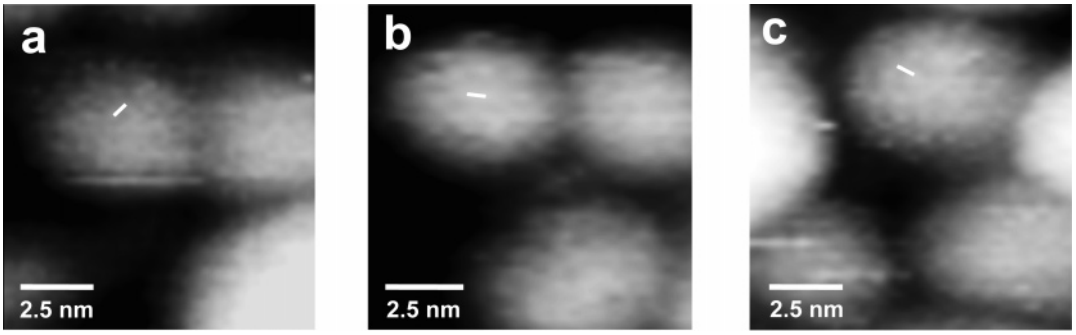

Figure 5. STM height images of an OT homoligand nanoparticle monolayer on Au foil illustrating consistency of headgroup spacing with tip velocity, but also showing image resolution changes with tip velocity. (a) Image of a group of nanoparticles whose headgroups are clearly visible when imaged at a tip velocity of 0.695 μm/s. The headgroup spacing on the nanoparticle ranges from 0.57 to 0.6 nm. (b, c) Images of two different areas from a single scan image that was imaged at 0.868 μm/s. (b) Same particles as in (a). In this case the imaging conditions are no longer optimal, and it is difficult to recognize individual headgroups on the nanoparticle. The few headgroups which can be recognized show a spacing of ~0.6 nm. (c) A separate group of nanoparticles whose headgroups are clearly visible, even at this increased scan speed, and that show spacings from 0.56 to 0.65 nm. The short, white lines in each image represent a single headgroup spacing measurement.

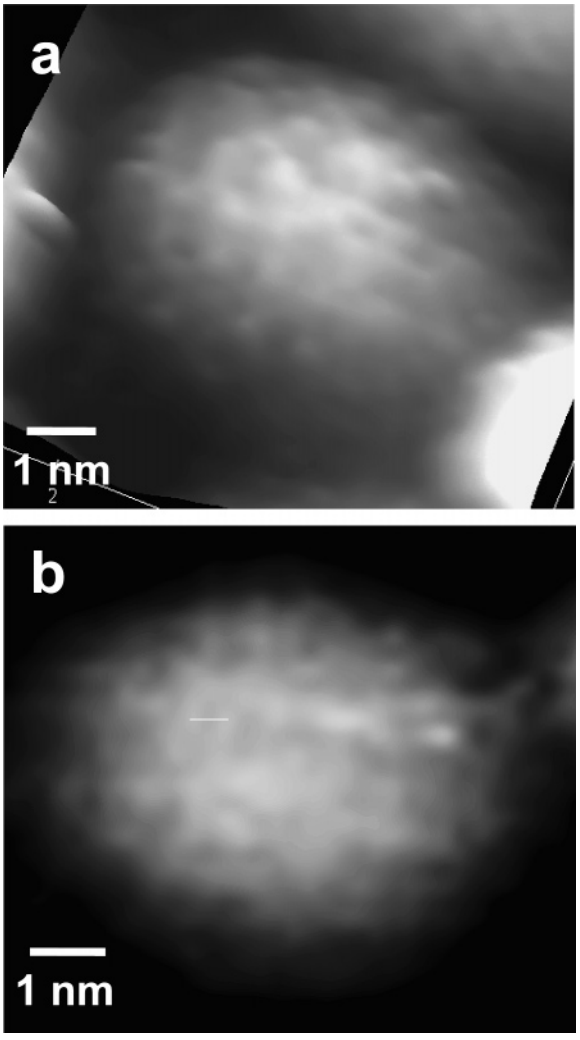

Figure 6. STM scan images of OT homoligand nanoparticles: (a) 3-D rendering of a homoligand nanoparticle in which the molecular headgroups are clearly visible; (b) example of a single headgroup spacing measurement. Several measurements were taken on each nanoparticle between clearly visible headgroups near the center of the particle. The measurements were typically taken horizontally between headgroups to minimize the effects of line scan artifacts or vertical drift during the imaging of the particle.

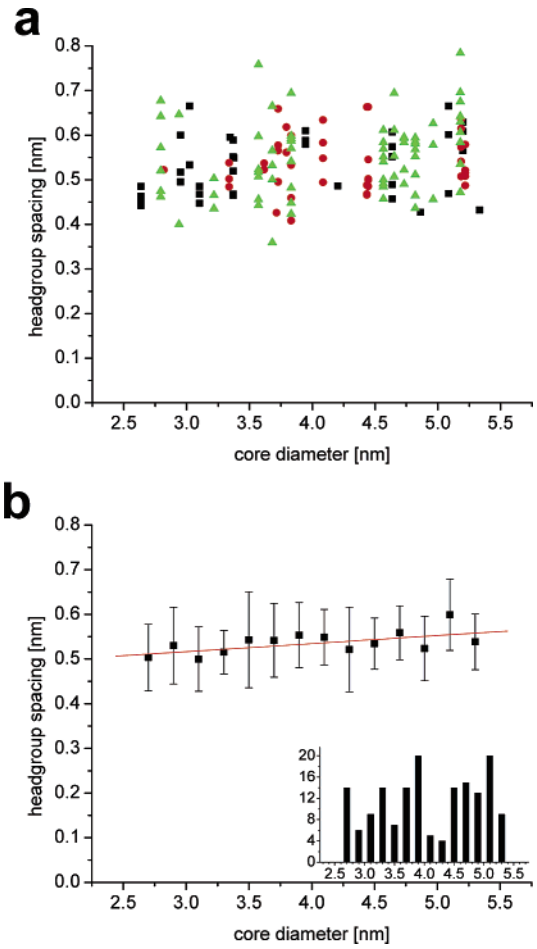

Figure 7. (a) STM headgroup spacing data from three scan images of OT homoligand nanoparticles as a function of core diameter: red circles, two-phase-synthesized nanoparticles, imaged at 0.868 μm/s; black squares, two-phase-synthesized nanoparticles imaged at 0.695 μm/s; green triangles, one-phase-synthesized nanoparticles imaged at a tip speed of 0.861 μm/s. (b) Averaged data from (a) showing a slight increase in headgroup spacing with core diameter. The red line is a linear fit to the data. The regression has statistical significance with a 99% confidence level ($R = 0.299$, DOF $= 164$, $R_{100} = 0.254$); the slope of the fit (2.7×10^{-2} nm/nm) is also significant with a 99.9% confidence level ($t = 3.99$, DOF $= 164$, $t_{120} = 3.37$). Inset: Histogram of the number of spacing measurements per nanoparticle core diameter.

foil exhibits a curvature comparable to that of the nanoparticle core, no ripples are observed, indicating that ripples are not the result of the STM tip scanning over an area of high curvature. If one now examines an image of several nanoparticles (Figure

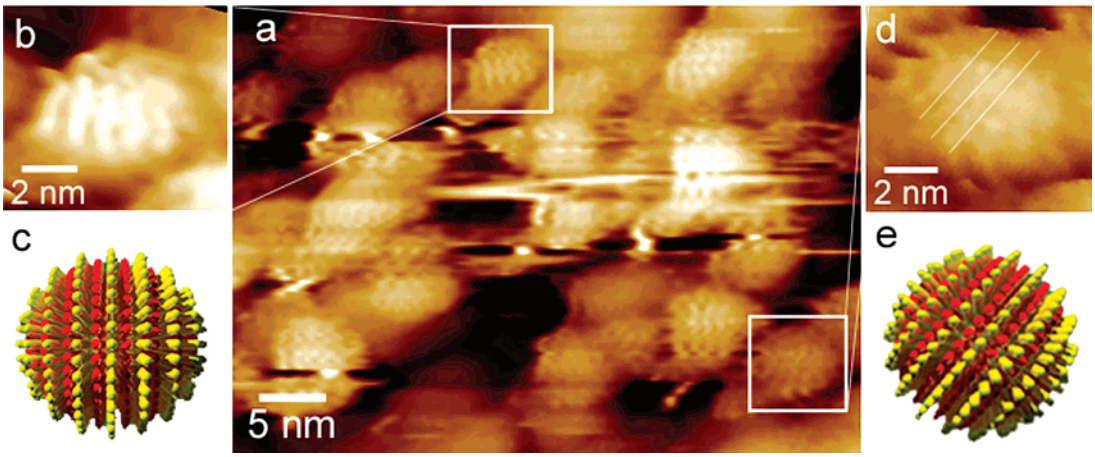

Figure 8. (a) STM height image of an OT/MPA (2:1) mixed-ligand nanoparticle monolayer on Au foil showing ripples in various orientations. (b) Enlarged image of a single nanoparticle and (c) corresponding schematic drawing showing molecular domains that align into parallel ripples that encircle and/or spiral around the nanoparticles. The spacing of the phases, measured as the average spacing between two peaks, is 0.89 nm. (d) Enlarged image and corresponding schematic drawing (e) of a nanoparticle with ripples oriented ~45° to the fast scan direction. This rotation results in reduced visualization of the particle's ripples.

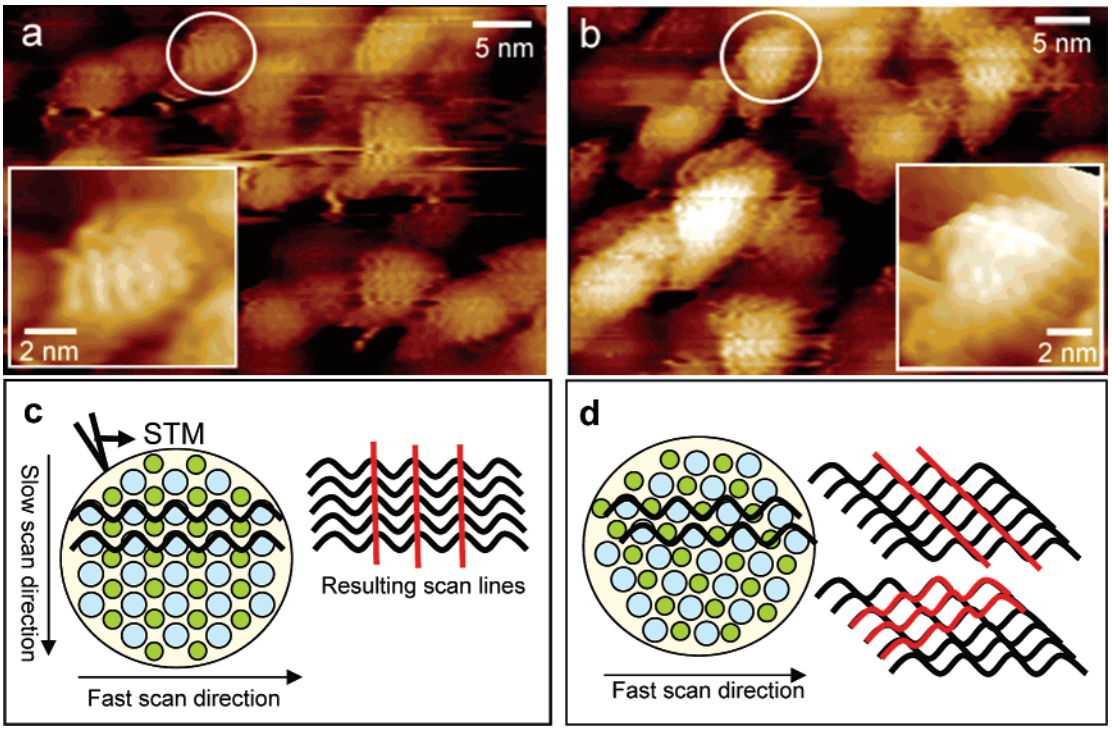

Figure 9. (a) STM height image of an OT/MPA (2:1) nanoparticle monolayer taken at a 0° scan angle. Inset: Enlarged image of a single nanoparticle showing ripples running perpendicular to the fast scan direction. (b) STM height image of the same sample as in (a) imaged at a 30° scan angle. Inset: Enlarged image of the same nanoparticle as in (a); however, the ripple direction is now difficult to discern. (c) Schematic drawing of STM imaging of the ligand lattice on a nanoparticle where the blue and green dots represent a phase-separated "rippled" arrangement of two different ligands. The drawing illustrates the resulting scan lines and ripple direction seen (shown in red) when ripples run perpendicular to the fast scan direction. (d) Schematic drawing similar to that in (c). The ligand shell molecular lattice has been rotated by 30°, resulting in two possible ripple directions being seen and giving rise to the characteristic crosshatched appearance on the particle when the two ripple directions are overlaid.

8), it is immediately evident that those particles with the most clear ripples (that is, ripples whose direction is easy to discern) almost always have domains which tend to run perpendicular, within ±30°, to the fast scan direction (or, equivalently, parallel to the slow scan direction). However, there are several other nanoparticles within the scan images that show nanostructuring, but whose ripples' direction is difficult to discern (Figure 8d). This disparity is likely due to how the tip scans across each ligand shell "lattice" and the resulting merging of scan lines.

When particles whose ripples are rotated so that they are not perpendicular to the fast scan direction are imaged, the imaging scan lines, when merged to form an image, can produce what appear to be two sets of crossing ripple directions, resulting in a crosshatched appearance on the nanoparticle ligand shell. This phenomenon is illustrated in Figure 9; we first imaged a sample at 0° scan angle and obtained crisp images of a nanoparticle whose ripples run perpendicular to the fast scan direction. We then rotated the sample by 30° and found that the particle's

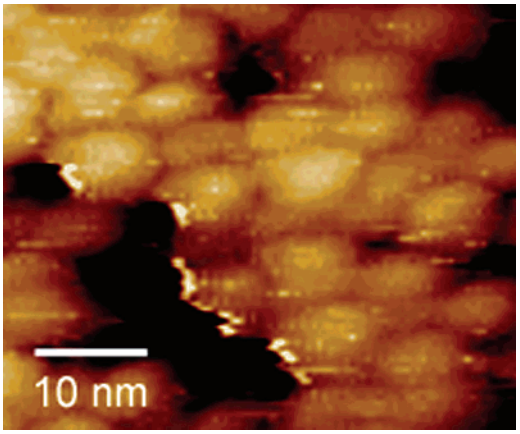

Figure 10. STM height image of a nonanethiol/mercaptohexanol (2:1) nanoparticle monolayer.

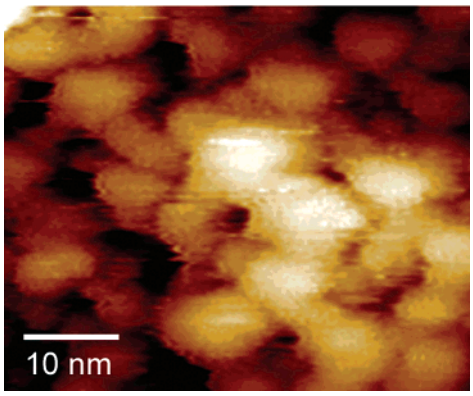

Figure 11. STM height images of an octanethiol/mercaptoundecanoic acid (1:1) nanoparticle monolayer.

ripple direction was now difficult to discern and exhibits the typical "crosshatching" of a rotated particle. We should state here that the experiment just described is extremely challenging because many elements must come together to make it possible. First, one needs to find an isolated nanoparticle in a condition where good images are achievable. Second, when the image is rotated, the always present sample drift must be minimal so that the particle stays within the field of view. Third, the new approach direction to the particle must not contain different topological hindrances to the STM tip. In general, rotated images of nanoparticle films are hard to interpret, due mostly to the fact that almost never does the same part of the image stay clear throughout the rotation. Typically, once we obtain a clear image of nanoparticles, our first priority is to obtain comparable images at different tip speeds; by the time this is achieved, often the tip quality has deteriorated to the point that further imaging is not possible or is unreliable.

To date, we have clearly observed ripple formation using several binary mixtures of ligands on gold nanoparticles ranging from 2.5 to 6 nm in core diameter. In all cases the chosen ligands contained a thiol end group to ensure significant mobility across the gold core and ability to undergo place exchange. Also, each combination of ligands was chosen such that each constituent's headgroup functionality and length differed significantly from those of the other to help drive the phase separation. Various rippled nanoparticles and their compositions are shown in Figures 10−12. Ripples were observed for nanoparticles coated with nonanethiol/mercaptohexanol (2:1), with an average spacing of approximately 0.7 nm, octanethiol/mercaptoundecanoic acid (1:1), with an average spacing ranging from 0.8 to 0.9 nm, and 4-aminothiophenol/hexanethiol (2:1), with an average ripple spacing ranging from 0.6 to 0.8 nm.

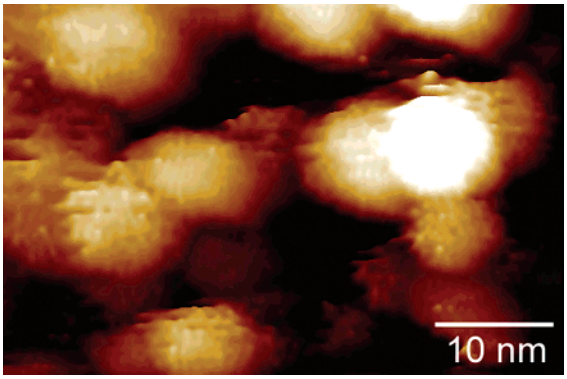

Figure 12. STM height images of a 4-aminothiophenol/hexanethiol nanoparticle monolayer.

3.4.2. Dependence of Ripple Spacing on Diameter. An in-depth study of ripple spacing as a function of core diameter was undertook for OT/MPA (2:1) nanoparticles as these particles have shown the best contrast between ripples (probably due to the fact that they present the largest ripple spacing observed to date) and hence provide the most accurate spacing data. Additionally, they have been imaged numerous times over a period of three years. Here we analyze data from two synthetic batches of the OT/MPA (2:1) nanoparticles (denoted as np1 and np2), synthesized using an identical two-phase procedure by two individuals. The two syntheses, although identical, led to nanoparticles with different polydispersities, with the core diameters of np1 ranging from 2 to 6 nm and those of np2 ranging from 3 to 8 nm. As shown in Figure 13a,b, we plot the STM-observed headgroup spacing as a function of core diameter (determined assuming that the longer OT molecules in the ligand shell determine the STM-observed diameter) for one individual scan image of np1 as well as a composite plot containing data from all individual scans. Overall we have noticed that when plotting the spacing from each individual scan image, clear trends are visible and that these trends stay qualitatively the same, even across images of nanoparticles synthesized on different occasions. Typically when these plots are combined, the trends seem to be washed out, but still visible. At present we believe that this is due to the increased number of outliers in the combined images and to the increased error bars of nanoparticles whose size is at the transition point (see the discussion below). Ripple spacing on the nanoparticles was measured near the center of each particle, averaging more than five measurements per particle. The average ripple spacing per diameter in each scan image typically ranges from 0.9 to 1.1 nm. The composite plot shows an overall average spacing of 1.04 nm with an increase in spacing with diameter from 1.00 nm at 1.7 nm core diameter to 1.07 nm at 5.9 nm. However, it should be noted that in all of the individual scans, and in the composite plot, there seems to be a decrease in ripple spacing from approximately 3.1 to 4.1 nm and from 4.5 to 5.5 nm core diameters, with what appears to be a transitional jump in spacing between the two in the region of 4.1−4.5 nm.

When the data from np2 are plotted in the same manner as for np1, similar trends and values emerge (Figure 13c,d). The average spacing measurements from each scan image of np2

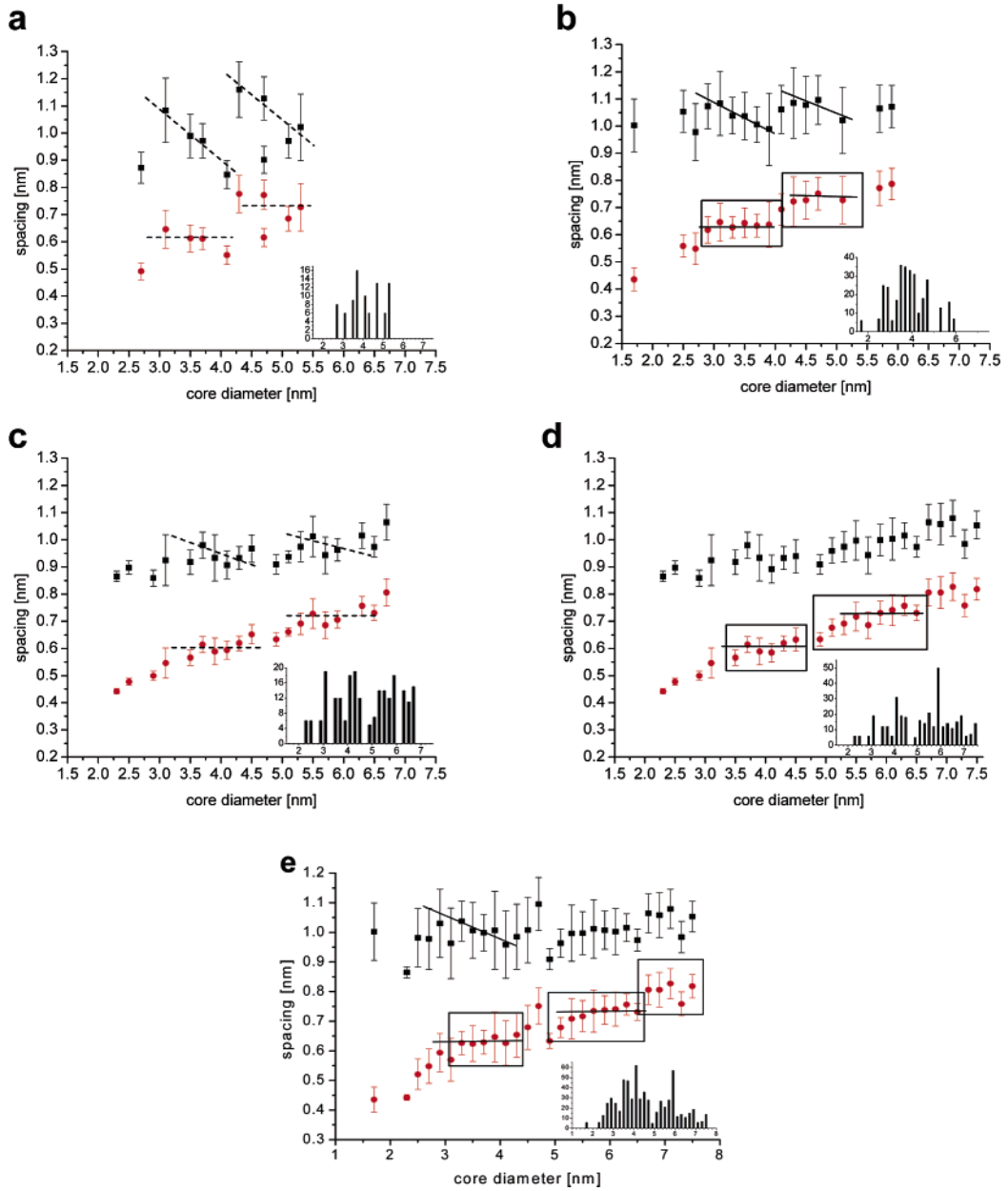

Figure 13. STM-observed headgroup spacing (black squares) and corresponding sulfur−sulfur spacing (determined using the continuous representation) (red circles) of OT/MPA (2:1) nanoparticles as a function of nanoparticle core diameter: (a) np1 data from one individual scan image and (b) a composite plot containing data from all individual scan images of np1; (c) np2 data from one individual scan image and (b) a composite plot containing data from all individual scan images of np2; (e) combined data from np1 and np2. The plots from single measurements show decreases in ripple spacing from roughly 2.9 to 4.5 nm and from roughly 5.3 to 6.7 nm, separated by discrete transitional increases in spacing. The trends in the plots from single images are quite easy to identify by the eye, and dotted lines have been superimposed to help guide the eye; they have not been calculated and should be considered as arbitrary. In the case of the statistically more relevant combined plots (b, d, e), the trend lines shown are supported by a statistical analysis. The differences in the average sulfur−sulfur spacings in the regions identified with boxes are significant with a level of confidence of 99% or more. The regression and the slopes of the trend lines in the headgroup spacing plots are significant with a level of confidence of 95% or more. Insets: histograms of the number of spacing measurements per nanoparticle diameter.

typically ranged from 0.85 to 1.10 nm and show a complex dependence on core diameter. The average ripple spacing for the composite data is 0.98 nm with an overall increase in spacing with diameter from 0.86 nm at 2.3 nm to 1.06 nm at 6.6 nm. Combining the data from np1 and np2 (Figure 13e) gives a more complete picture of OT/MPA (2:1) ripple spacing. The overall average headgroup spacing is 1.04 nm, increasing from 1.00 nm at 1.7 nm to 1.05 nm at 7.5 nm.

We began a preliminary study of the dependence of ripple spacing on core diameter for rippled OT/MPA (1:1) nanoparticles to examine whether those spacing trends observed for OT/MPA (2:1) nanoparticles hold true for other ligand compositions. As shown in Figure 14, both the individual and composite spacing plots show spacings that have a clear dependence on diameter. As shown in the composite plot, there is an overall increase in ripple spacing from 0.58 nm at 1.5 nm core diameter to 0.75 nm at 5.7 nm and an overall average spacing of 0.69 nm.

To demonstrate the independence (or better very shallow dependence) of ripple spacing on tip speed, we analyzed and compared the spacing on nanoparticles from two scan images of OT/MPA (1:1) nanoparticles: one imaged at 0.57 μm/s and

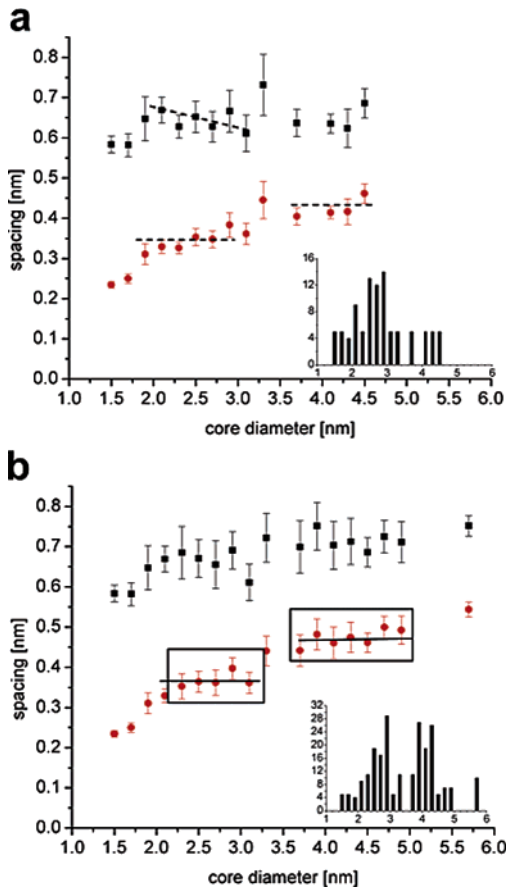

Figure 14. STM-observed headgroup spacing and corresponding sulfur−sulfur spacing of OT/MPA (1:1) nanoparticles as a function of nanoparticle core diameter. (a) shows data from one individual scan image. (c) Combined data from all individual scan images. Insets: histograms of the number of spacing measurements per nanoparticle diameter. The plot from a single measurement (a) shows decreases in ripple spacing in the ranges of 2.1−3.1 and 3.3−4.9 nm core diameters separated by a jump in spacing in the region of 3.1−3.3 nm core diameter. The trends in (a) have been superimposed to help guide the eye; they have been not calculated and should be considered as arbitrary. In the case of the combined plot (b), the differences in the average sulfur−sulfur spacings in the regions identified with boxes are significant with a level of confidence of 99%.

the other at 0.814 μm/s (Figure 15). As can be seen, the two plots of ripple spacing as a function of diameter are roughly overlaid, with any deviation between the two likely due to measuring rotated particles and of noise erroneously interpreted as real features. A total of 153 particles were analyzed, with an average of ∼5.9 measurements per particle, resulting in 902 spacing measurements analyzed. In this case, the error bars are ±1 standard deviation of the average of all of the average spacing measurements for particles of a given diameter, which was typically ∼0.5 Å.

4. Discussion

Our images show that the arrangement of molecules in the 3-D self-assembled monolayers that constitute the nanoparticles' ligand shell is different from what has been shown in the literature to be the arrangement of those same molecules on flat Au(111) and Au(100) surfaces.[78,79] For Au(111), the molecules pack in a hexagonal lattice with an interchain spacing

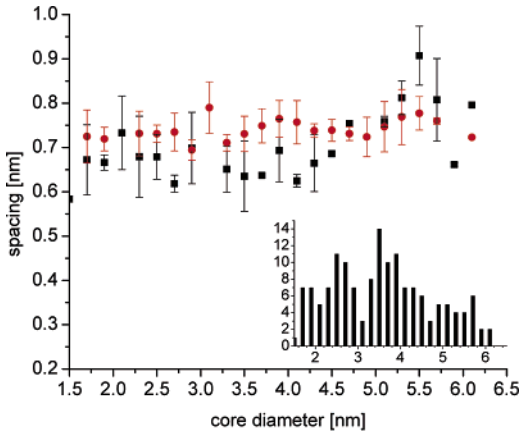

Figure 15. Comparison of the STM-observed headgroup spacing of OT/MPA (1:1) nanoparticles for varying STM tip velocities. Plotted is the observed headgroup spacing as a function of core diameter from two scan images: one taken at 0.57 μm/s (black squares) and the other at 0.814 μm/s (red circles); the overall average spacing was found to be 0.70 nm ± 0.10 nm and 0.74 nm ± 0.05 nm, respectively. Note that the error bars are ±1 standard deviation of the average of all of the average spacings for particles of a given diameter. Inset: histogram of the number of nanoparticles measured per nanoparticle diameter.

of 5.0 Å;[71,80] on flat Au(100), the packing is still debated, with experimentally observed interchain distances ranging from 4.54 Å, for a square lattice,[81] to 5.77 and 4.81 Å, for a distorted, hexagonal lattice. If the arrangements were the same, no dependence of headgroup spacing on core diameter should have been observed. The case of homoligand nanoparticles is different from the case of mixed-ligand ones, with the latter being more complicated to interpret (but easier to image) due to the formation of ribbonlike phases of molecular dimensions.

4.1. Homoligand Nanoparticles. Imaging homoligand nanoparticles is challenging; often good images can be obtained only in a narrow tip speed range, and outside of that range images become blurry and molecular resolution is lost. However, to unambiguously assign the observed structure on a nanoparticle to molecular arrangements (as opposed to random noise), images at different tip speeds need to be obtained. For the particles examined here, we have been able to do this on at least two separate occasions. The plot in Figure 7 shows headgroup spacing as a function of core nanoparticle diameter. The variation in individual headgroup spacing values per nanoparticle is due to the nature of the measurement. It is often the case that a nearest neighbor headgroup is missing in our images; this can be due to a defect in the monolayer or a problem in imaging. This results in measuring two headgroups that are not nearest neighbors. To not bias our analysis, we included these larger spacings even if they were double the average ones. The observed average headgroup spacing (S) was 5.4 Å and varied with particle diameter from 5.1 Å at 2.7 nm diameter to 5.6 Å at 5.5 nm core diameter (Figure 7).

To correlate the STM-observed headgroup spacing to the actual packing arrangements of ligands around the core, we considered two basic models. First we used the simplest model of ligand packing—the crystallographic model (Figure 16a). Gold nanocrystals typically have surfaces composed of small (111) and (100) facets.[82] Locally the facets are flat, so it could be assumed that the molecular arrangement of alkanethiols on

(78) Poirier, G. E.; Tarlov, M. J.; Rushmeier, H. E. *Langmuir* **1994**, *10*, 3383−3386.
(79) Ulman, A.; Eilers, J. E.; Tillman, N. *Langmuir* **1989**, *5*, 1147−1152.
(80) Poirier, G. E.; Tarlov, M. J. *Langmuir* **1994**, *10*, 2853−2856.
(81) Strong, L.; Whitesides, G. M. *Langmuir* **1988**, *4*, 546−558.

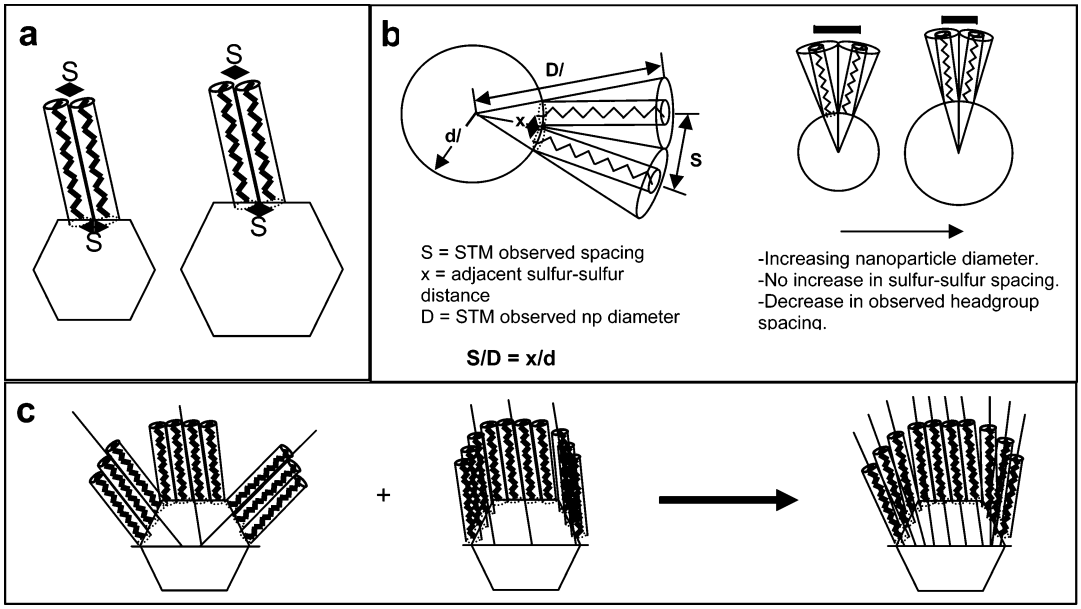

Figure 16. (a) Simplest representation of ligand packing for homoligand nanoparticles. Ligands pack on each nanoparticle facet as they would on a crystallographically equivalent flat 2-D gold surface, with a headgroup spacing corresponding exactly to the sulfur−sulfur spacing of the ligands at the nanoparticle core. (b) Schematic illustration of a ligand-coated nanoparticle relating the STM-observed headgroup spacing (*S*) at the periphery to the corresponding sulfur−sulfur spacing (*x*) at the nanoparticle core. (c) Ligands have essentially two configurations that they can assume on the faceted core: (i) they can assume their optimal tilt angle with regard to each facet (left), or (ii) they can assume a global tilt angle (middle). The first configuration leads to high-energy defects at the crystal edges, while the second does not take advantage of the particle curvature. Hence, the true configuration is likely a compromise between the two, with the ligands roughly conforming to a global tilt angle, but relaxing, and splaying outward as shown in the rightmost drawing in (c).

these facets would resemble that on corresponding flat surfaces. In this case, the STM-observed headgroup spacing (*S*) of adjacent ligands should equal the sulfur−sulfur spacing (*x*) of the ligands at the nanoparticle core and should (to a first approximation) not be dependent on nanoparticle diameter. Alternatively, one could represent the particles as spheres with molecules that radially extend out of the core shell with their sulfur groups packing tightly at the core and their headgroups loosely packed at the particle's outer boundaries (see Figure 16b for a drawing adapted from Luedtke and Landman).[83] This representation will be referred to hereafter as the continuous model, as done by Murray and co-workers.[33] Here, headgroup spacing (*S*) is related to the spacing of the corresponding sulfur atoms (*x*) at the gold nanocrystal surface by a simple geometric relation: $S/D = x/d$, where *d* is the particle diameter and *L* is the ligand length. In the case of our experimental data, the STM images contain both *D* and *S*, while *d* and *x* have to be derived. *L* was determined by assuming an all-trans configuration of the alkane chains, in agreement with IR data and molecular modeling results.[83] Unlike in the crystallographic model, here the STM-observed headgroup spacing (*S*) of adjacent ligands should be larger than the sulfur−sulfur spacing (*x*) of the ligands at the nanoparticle core and should be dependent on nanoparticle diameter.

Murray and co-workers tested nanoparticle ligand coverage data, obtained through the combination of thermal gravimetric analyses with TEM images, against both the crystallographic and the continuous representations described above.[33] It is known that alkanethiols form commensurate $\sqrt{3}\times\sqrt{3}R30°$ lattices on flat Au(111) surfaces;[84] thus, their coverage (defined as the ratio of ligands to surface gold atoms) is 33%. Murray found that on nanoparticles the coverage was consistently larger (up to 66%). This is not surprising in the continuous model as tighter packing is allowed at the core surface by the larger area that is available for the headgroups due to splay of the molecules. In the crystallographic model, the larger coverage could be explained assuming 33% coverage on the crystalline facets and 100% coverage at the facet edges. Thus, here we refine our previous description of the crystallographic model to include ligands at facet edges, the presence of which leads to an increase in the monolayer density (and consequently surface coverage).

Considering the continuous model, headgroup spacing should decrease with diameter, ultimately becoming identical to the sulfur−sulfur spacing, i.e., the headgroup spacing on flat surfaces. Importantly, in this model, sulfur−sulfur spacing should be independent of diameter. For the crystallographic model, it is not true that the *average* headgroup spacing is independent of diameter if it is assumed that all edges are occupied by ligands. Indeed the observed average headgroup spacing will be a weighted average of the spacing on facets and that at facet boundaries (i.e., edges), which are highly crowded, and it should increase (not considering curvature effects) with diameter toward its value on flat (edgeless) surfaces.

Our data are not in full agreement with either of these models. First, headgroup spacing increases with diameter (as expected from the crystallographic model), but it is always larger than that of ligands on flat surfaces. Second, sulfur−sulfur spacing (*x*) is not independent of diameter; however, when it is plotted against particle diameter (for the OT nanoparticles, see Figure 17), it is possible to see two regions of relatively constant spacing emerge. It should be noted that the average sulfur−

(82) Zanchet, D.; Hall, B. D.; Ugarte, D. *J. Phys. Chem. B* **2000**, *104*, 11013−11018.
(83) Landman, U.; Luedtke, W. D. *Faraday Discuss.* **2004**, *125*, 1−22.
(84) Ulman, A. *Chem. Rev.* **1996**, *96*, 1533−1554.

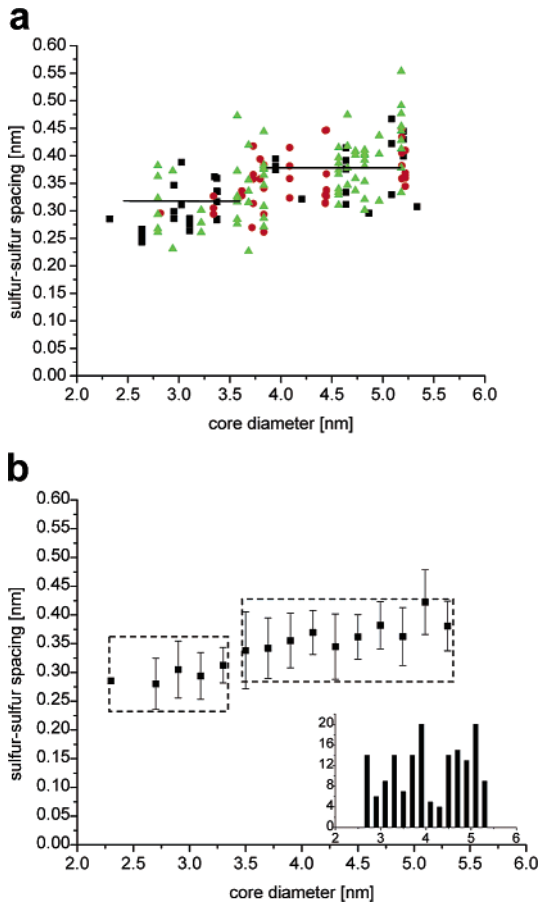

Figure 17. (a) Sulfur−sulfur spacing (calculated using the continuous representation) of OT homoligand nanoparticles from three STM scan images as a function of core diameter: red circles, two-phase-synthesized nanoparticles, imaged at 0.868 μm/s; black squares, two-phase-synthesized nanoparticles imaged at 0.695 μm/s; green triangles, one-phase-synthesized nanoparticles imaged at a tip velocity of 0.861 μm/s. (b) Averaged data from (a) showing an increase in sulfur−sulfur spacing with core diameter. The dotted rectangular boxes outline two possible flat regions of sulfur−sulfur spacing in the regions of 2.3−3.3 and 3.5−5.5 nm core diameters. The difference in average spacing in these two regions is statistically significant with a level of confidence of 99%. Inset: histogram of the number of spacing measurements per nanoparticle core diameter.

sulfur spacings ($\langle x \rangle$), ranging from 2.8 to 4.2 Å, are in close agreement to those found by Landman and co-workers,[55] who used molecular dynamics simulations to model the equilibrium assembly of dodecanethiol-coated Au_{1289} nanoparticles (~3.3 nm) and found that the distribution of sulfur−sulfur spacings (here called x) on the (111) facets was broad, with a peak at ~4 Å, and skewed toward larger values, the average spacing being 4.4 ± 0.4 Å. On the (100) facets of the crystalline core, the average sulfur−sulfur distance was 4.1 ± 0.3 Å. The present agreement could be coincidental. A systematic study of homoligand nanoparticles coated with alkanethiols of different lengths that could provide insight into this matter is under way.

To develop an appropriate model for ligand packing around the nanoparticle core, it is useful to consider our data in light of the two proposed ligand shell representations in more detail. Neither representation is realistic, and while our data do not agree with either completely, they could be qualitatively "forced" to agree with either as well. The observed average headgroup spacing is larger than the spacing of the same molecules on flat surfaces, something that is not possible to explain with a simple 2-D-like packing. Additionally, a known property of SAMs is that molecules arrange themselves with a tilt angle relative to the surface normal to maximize packing (i.e., van der Waals interactions between chains).[79] Assuming that the packing on flat surfaces and on nanoparticle facets is the same would mean that on each facet the molecules arrange with a given tilt angle, generating a large number of line defects at the facet edges (Figure 16a). A large number of high-energy defects would then be generated, something that goes against basic thermodynamic intuition. Landman and co-workers predicted that below the molecules' melting temperature a global molecular arrangement results with ligands assuming a single tilt angle relative to a single diameter of the core (per topological hemisphere)[55] as shown in Figure 16c. Other molecular dynamics simulations have also found that thiol molecules, coating ~5 nm gold nanoparticles, induce an isotropic surface energy, resulting in a somewhat rounded shape of the particle.[56] Furthermore, our STM images of nanoparticles[67] and those of others[64,85,86] show spherical objects with no hint of facets, indicating that the molecular arrangements average out the crystallographic nature of the core, suggesting a global relaxation of the ligands on the particle core.

In considering the second representation, a sulfur−sulfur spacing (x) independent of nanoparticle size should be observed. Our data do not seem to conclusively show this. This representation also has the flaw that the particles are simply not spheres. However, nanoparticles are topological spheres, and indeed, molecules feel them as 3-D closed objects[54] —arguably more so the smaller the particles. Hence, molecules will tend to "splay" and find more space for their headgroups (relative to their sulfurs) the smaller the diameter, even if the core has a crystalline polyhedral shape. This is probably the reason for the extremely shallow dependence of x on diameter and for the headgroup spacing being larger than that on flat surfaces.

At present, we believe that the most probable equilibrium conformation for the ligand shell structure is a combination of the crystallographic model, with all of the ligands in one hemisphere assuming a similar tilt angle, and the continuous model, with some splay implicit in the curvature of the core, as shown in Figure 16c. In this case headgroup spacing should increase with diameter as the ratio between facet area and edge length increases and should always be larger than that on flat surfaces. Note that this ratio should linearly increase as the diameter increases, but changes in the crystallographic shape of the nanoparticle core will result in a discontinuous increase in such a ratio and should be reflected in a discontinuous increase in the observed headgroup spacing. Our data have a noise level that do not allow for a conclusive picture of the molecular arrangements; however, the trends observed (see also the discussion for mixed ligands) support this conclusion.

4.2. Mixed-Ligand Nanoparticles. When certain mixtures of thiolated molecules assemble on flat surfaces, phase separation occurs.[68−70,87] This is the case for many molecular combinations but is not a general property of mixed SAMs. It is easy to envision cases in which entropy-dominated assembly

(85) Osman, H.; Schmidt, J.; Svensson, K.; Palmer, R. E.; Shigeta, Y.; Wilcoxon, J. P. *Chem. Phys. Lett.* **2000**, *330*, 1−6.
(86) Gusev, A. O.; Taleb, A.; Silly, F.; Charra, F.; Pileni, M. P. *Adv. Mater.* **2000**, *12*, 1583−1587.
(87) Laibinis, P. E.; Nuzzo, R. G.; Whitesides, G. M. *J. Phys. Chem.* **1992**, *96*, 5097−5105.

would lead to homogeneous mixtures. Phase separation does occur for octanethiol and mercaptopropionic acid.[67] When these molecules assemble on gold nanoparticles, they still phase separate as they do on flat surfaces, but they form much smaller domains characterized by highly ordered arrangements.[67] It is better to clarify that, at this scale, it is not possible to apply a rigorous thermodynamic definition of "phase" anymore, and the arrangements in the particle ligand shell could easily be classified as the formation of ordered heterogeneous mixtures. We prefer to use the term "phase separation" to relate to the literature of mixed monolayers on flat surfaces.[68−71] It is too early to say whether all the mixtures that phase separate on flat surfaces form these ordered domains on gold nanoparticles, but as Figures 10 to 12 show, this seems to be the case for the particles studied to date.

We started to study the dependence of phase thickness (domain spacing) on core diameter. As discussed above, domain spacing measurements are affected by the uncertainty caused by the unknown angle of the domain axis relative to the imaging fast scan direction. As this angle decreases (that is, as ripples run closer to parallel to the fast scan direction) image quality deteriorates. Thus, the majority of the particles measured have domain angles that are typically close to normal to the scan direction and so have clearly defined ripples. By looking at Figures 13 and 14, it can immediately be noticed that, for both OT/MPA (2:1) and OT/MPA (1:1) nanoparticles, (i) the overall ripple spacing increases slightly with diameter and (ii) in most plots (mainly the ones from a single image) regions of negative slope separated by discontinuous jumps in spacing can be observed. Typically, at, or close to, the diameters where spacing jumps are observed, the error in the measurement increases. Overall changes in ripple spacing are fairly small, suggesting that the domain molecular composition, i.e., the number of molecules that determine the ripple thickness, does not change in the range of sizes studied in this work.

OT/MPA (1:1) nanoparticles exhibit a behavior that is less pronounced as compared to that shown by OT/MPA (2:1) particles, likely due to the decreased width of the ripples, making imaging and subsequent spacing analysis more difficult. When the continuous representation for both types of particles is applied (Figures 13 and 14), a steplike pattern in the sulfur−sulfur spacing plot seems to be present. Hence, this representation holds in the ranges of diameters where sulfur−sulfur spacing is constant. Transitional jumps in behavior were also observed by Murray and co-workers, who studied dodecanethiol-coated gold nanoparticles ranging in diameter from 1.5 to 5.2 nm.[22] They found, using TGA and FTIR, that the ligand shell monolayer underwent a transition in packing at a "critical" core diameter of ∼4.4 nm, with the larger particles exhibiting a more ordered, 2-D-like monolayer structure. The agreement between nanoparticles of the trends described above is remarkable, not only qualitatively, but also in the size ranges where the discontinuous upward transitions occur. Specifically, these particles and the OT homoligand ones have shown spacing jumps for core diameters in the ranges of 2.9−3.3 and 4.7−5.1 nm.

Some preliminary conclusions can be drawn from these plots. In all the particles studied here similar trends were observed (Figure 18). (i) Changes in ripple spacing occurred at similar diameter ranges, namely, in the ranges of 2.9−3.3 and 4.7−5.1 nm. The fact that these changes occur at similar diameters

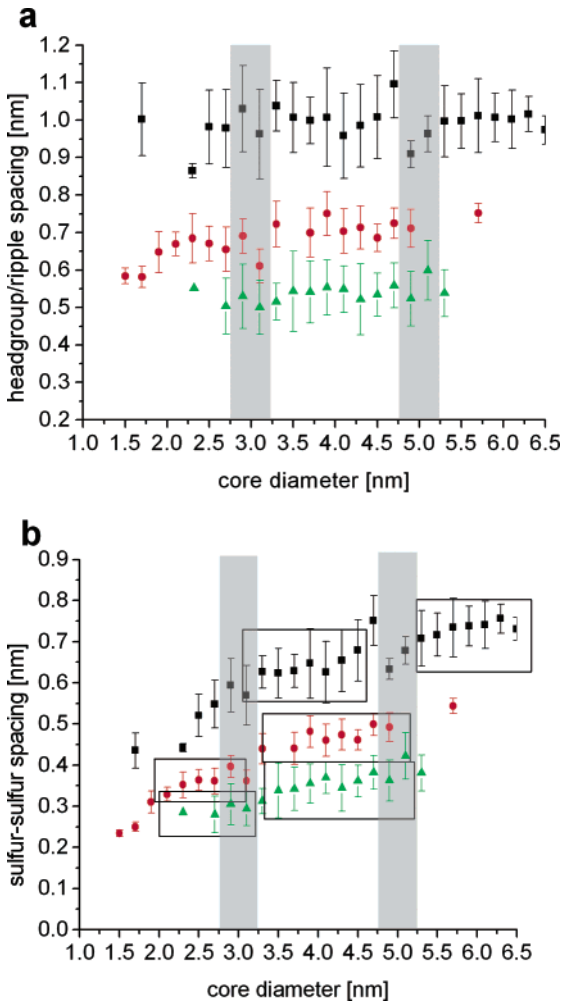

Figure 18. (a) Headgroup spacing as a function of core diameter for all nanoparticle compositions. Gray areas indicate regions of transitional changes in spacing. (b) Sulfur−sulfur spacing as a function of core diameter for all nanoparticle compositions. Boxes outline regions of constant spacing for each nanoparticle composition. Gray areas are the same as those for (a).

suggests that there is an effect driven by the shape/crystallographic nature of the metallic core. Indeed, it is known that when particles exceed a diameter of 2−3 nm, the predominant icosahedral shape of the particle core tends to become less frequent at the expense of the truncated dodecahedral one; for particles larger than 4 nm the truncated octahedral shape is the most common.[82,88] As discussed for the homoligand case, the spacing of the ligands is determined by the fraction of ligands that are on a flat facet relative to the fraction on the edges. As shape changes occur, this ratio has discontinuous jumps that can lead to discontinuous jumps in the ligand spacing. This effect translates from homoligand to mixed-ligand particles. (ii) Headgroup/ripple spacing overall increases with diameter. Increases in particle size lead to decreases in the fraction of edge atoms on the core surface and to the consequent decrease of ligands on edge atoms. These latter ligands are the ones that occupy crowded regions of space and lead to smaller headgroup spacing, so as their fraction decreases, the headgroup (and consequent ripple spacing) increases. (3) There are ranges in diameter where apparently ripple/headgroup spacing decreases.

(88) Cleveland, C. L.; Landman, U.; Shafigullin, M. N.; Stephens, P. W.; Whetten, R. L. *Z. Phys. D: At., Mol. Clusters* **1997**, *40*, 503−508.

In those regions, the sulfur−sulfur spacing, obtained using the continuous model, seems to be constant. Thus, we believe that this effect could be due to the curvature-driven splay of ligands that decreases as size increase. (iv) In the ranges of diameters studied ripple composition is not dependent on size.

4. Conclusions

In summary, using STM, we have been able to attain molecular level resolution images of the ligand shells of homoligand OT and mixed-ligand OT/MPA nanoparticles. We have shown that there are significant differences in morphology and packing density between the monolayer that constitutes the ligand shell of nanoparticles and monolayers of identical composition assembled on flat surfaces. We find that, for homoligand and mixed-ligand nanoparticles, headgroup spacing and domain spacing, respectively, are dependent on nanoparticle core size, increasing with particle diameter. Mixed-ligand particles show jumps in headgroup and domain spacing at critical nanoparticle core diameters in the ranges of 2.9−3.3 and 4.7−5.1 nm in the three particle types studied, indicating fundamental changes in ligand packing. These measurements are a first step toward developing a complete picture of the 2-D molecular arrangement present within the 3-D ligand shell of nanoparticles. Combined with the ability to control morphology through composition, they represent an achievement toward developing a curvature-based phase diagram for monolayers of various compositions.

5. Experimental Section

All of the chemicals and gold foils were purchased from Sigma-Aldrich and used as received. Au(111) thermally evaporated on mica was purchased from Molecular Imaging. Epoxy glue, Epo-tek 377, was purchased from Epoxy Technology.

5.1. Nanoparticle Synthesis. 5.1.1. Two-Phase Method. $HAuCl_4 \cdot 3H_2O$ (354.45 mg, 0.9 mmol) was dissolved in 50 mL of water and the resulting solution stirred for 10 min. A 4-fold excess of $(BrN((CH_2)_7CH_3)_4$ (2.187 g, 4 mmol) was dissolved in 80 mL of toluene, the resulting solution added to the aqueous phase, and the mixture allowed to stir for 30 min, or until the color due to the gold salt had transferred completely to the organic phase. The thiolated molecule (or a mixture of thiolated molecules) (0.9 mmol) was injected into the solution and allowed to react for 20 min, after which the solution typically attained a white color. A 30 mL portion of a 0.33 M water solution of $NaBH_4$ was added slowly dropwise until the solution became a deep red color, and then the drop rate was increased to ∼1 drop/s. After 2 h of stirring, the phases were separated, and the organic phase was washed three times with water, then reduced to 10 mL, and diluted with ∼80 mL of ethanol. The solution was left in the refrigerator overnight to allow for the nanoparticles to slowly precipitate. The particles were collected by vacuum filtration using a quantitative paper filter and washed extensively with water, ethanol, acetonitrile, and acetone. Typically the collected black powder weighed ∼100 mg. Nanoparticles that were soluble in ethanol were collected by vacuum evaporation of the ethanol solution and extensive rinsing with water, acetone, and toluene.

5.1.2. One-Phase Method. The entire reaction was performed at 0 °C. To 500 mL of absolute ethanol was added $HAuCl_4 \cdot 3H_2O$ (354.45 mg, 0.9 mmol), and the resulting mixture was stirred for 10 min. The thiolated molecule (or a mixture of thiolated molecules) (0.9 mmol) was injected into the solution and allowed to react for 20 min. A 200 mL portion of a supersaturated solution of $NaBH_4$ in ethanol was then added slowly dropwise until the solution became a deep red color, and then the drop rate was increased to ∼1 drop/s. After complete addition, the solution was stirred for 2 h and then transferred to the refrigerator to slowly precipitate. The particles were then isolated and cleaned as described for two-phase synthesis.

5.1.3. Octanethiol-coated nanoparticles were synthesized using both the one-phase method (128.3 mg) and the two-phase method (131.55 mg).

5.1.4. Nonanethiol/mercaptohexanol (2:1)-coated nanoparticles were synthesized using the one-phase method with nonanethiol (96.2 mg, 0.60 mmol) and mercaptohexanol (40.3 mg, 0.30 mmol).

5.1.5. Octanethiol/mercaptopropionic acid (2:1)-coated nanoparticles were synthesized using the one-phase method with OT (87.8 mg, 0.60 mmol) and MPA (31.8 mg, 0.30 mmol).

5.1.6. Octanethiol/mercaptopropionic acid (2:1)-coated nanoparticles (np2) were synthesized using the two-phase method with OT (92.3 mg, 0.63 mmol) and MPA (34.2 mg, 0.32 mmol).

5.1.7. Octanethiol/mercaptopropionic acid (2:1)-coated nanoparticles (np1) were synthesized using the 2-phase method with OT (87.5 mg, 0.60 mmol) and MPA (37.4 mg 0.35 mmol).

5.1.8. 4-Aminothiophenol/hexanethiol (2:1)-coated nanoparticles were synthesized using the 2-phase method with 4-aminothiophenol (74.83 mg, 0.6 mmol) and hexanethiol (35.65 mg, 0.3 mmol).

5.1.9. Octanethiol/mercaptoundecanoic acid (1:1)-coated nanoparticles were synthesized using the one-phase method.

5.2. Formation of the Au on Glass Substrate. Au(111) thermally evaporated on mica (Molecular Imaging) was attached to a clean glass microscope slide, gold side down, using a thin layer of epoxy glue. The mica/gold/epoxy/glass sandwich was cured overnight at 150 °C and then immersed in a 200 μM ethanolic solution of octanedithiol for 2 h. The mica could then be cleaved from the underlying gold, resulting in a flat, monolayer-coated gold surface supported on glass. The gold on glass was reimmersed into the dithiol solution for several more hours to further complete the monolayer formation. Afterward, the substrate was washed repeatedly with ethanol and dried under nitrogen.

5.3. Formation of a Nanoparticle Monolayer on Au on Glass. A 2 mg portion of nanoparticles was dissolved in 10 mL of an appropriate solvent (ethanol or toluene depending on solubility), and a few drops of the solution were cast onto the gold substrate and allowed to slowly, but not completely, evaporate in saturated solvent vapor overnight. The substrate was then rinsed with toluene and ethanol and dried under nitrogen.

Acknowledgment. We are extremely grateful to Vincenzo Vitelli and David Nelson for helpful discussions and to Andrea Centrone and Jacob W. Myerson for the synthesis of some of the particles shown. The financial support of the National Science Foundation (Grant NIRTDMR-0303973) and of the Petroleum Research Fund are kindly acknowledged. F.S. is grateful to 3M and to DuPont for young faculty awards. A.M.J. acknowledges support from the Collamore Fellowship for graduate students.

JA061545H